Journal of Biomedical Optics

SPIEDigitalLibrary.org/jbo

Feasibility of interstitial near-infrared radiance spectroscopy platform for *ex vivo* canine prostate studies: optical properties extraction, hemoglobin and water concentration, and gold nanoparticles detection

Serge Grabtchak
Logan G. Montgomery
William M. Whelan

SPIE

Feasibility of interstitial near-infrared radiance spectroscopy platform for *ex vivo* canine prostate studies: optical properties extraction, hemoglobin and water concentration, and gold nanoparticles detection

Serge Grabtchak,[a,b,c,*] Logan G. Montgomery,[a] and William M. Whelan[a,d]
[a]University of Prince Edward Island, Department of Physics, 550 University Avenue, Charlottetown, Prince Edward Island C1A 4P3, Canada
[b]Dalhousie University, Department of Electrical and Computer Engineering, Halifax, Nova Scotia B3H3J5, Canada
[c]Dalhousie University, Department of Physics, Halifax, Nova Scotia B3H3J5, Canada
[d]Atlantic Veterinary College, Department of Biomedical Sciences, Charlottetown, Prince Edward Island C1A 4P3, Canada

Abstract. The canine prostate is a close match for the human prostate and is used in research of prostate cancers. Determining accurately optical absorption and scattering properties of the gland in a wide spectral range (preferably in a minimally invasive way), linking optical properties to concentrations of major endogenous chromophores, and detecting the presence of localized optical inhomogeneities like inclusions of gold nanoparticles for therapeutic and diagnostic purposes, are among the major challenges for researchers. The goal of the article is to demonstrate a feasibility of the multifunctional radiance spectroscopy platform in providing the required information. For *ex vivo* canine prostate, extraction of the effective attenuation and diffusion coefficients using relative cw radiance measurements was demonstrated in the 650- to 900-nm range. The derived absorption coefficient was decomposed to contributions from 9.0 μM HbO_2, 29.6 μM Hb, and 0.47 fractional volume of H_2O. Detection of a localized inclusion containing $\sim 1.5 \cdot 10^{10}$ gold nanorods (0.8 μg Au) at 10 mm distance from the urethra was achieved with the detector in the urethra and the light source in a virtual rectum position. The platform offers the framework for a systematic study of various chromophores in the prostate that can be used as comprehensive diagnostic markers. [DOI: 10.1117/1.JBO.19.5.057003]

Keywords: radiance; canine prostate; optical properties; hemoglobin; gold nanoparticles.

Paper 140099R received Feb. 19, 2014; revised manuscript received Apr. 4, 2014; accepted for publication Apr. 4, 2014; published online May 1, 2014.

1 Introduction

In spite of some differences,[1–4] canine prostate is the closest match for the human prostate and is widely used in research studies. It is also considered the best model for human prostate cancer,[5] even though there is no implanted prostate cancer model in dogs, and most studies are done on the benign prostate.[6] It is often used for evaluation of various prostate ablative techniques like photodynamic therapy (PDT)[7] and thermal therapy.[8]

The importance of knowing the optical properties of biological tissues, in general, and canine prostate, in particular, can be hardly overestimated since "... specifying the optical properties of a tissue is the first step toward properly designing devices, interpreting diagnostic measurements or planning therapeutic protocols."[9] The main purpose for measuring optical properties of canine prostate has been for treatment planning and monitoring during PDT because absorption and scattering properties of the tissue determine the light fluence distribution in the target volume.[10] As a result, current knowledge of optical properties of canine prostate is restricted by several discrete wavelengths.[10–19]

In laser prostatectomy, the extent of thermal coagulation of tissue also depends on the optical properties. It was shown for *in vitro* canine prostate tissues that thermal coagulation changes optical properties of the tissue: the absorption coefficient decreases and the scattering coefficient increases as compared with nontreated tissue.[11] The change in the optical properties was shown to be wavelength-dependent. Hence, knowledge of spectrally resolved absorption and scattering coefficients is essential for knowing light distribution in the tissue and, as a result, predicting the extent of the thermal damage to the tissue. However, measurements of optical properties are typically done at the wavelength of light at which the treatment is performed and, thus lack spectral information.

Moving from a single wavelength to spectroscopic measurements has been an increasing trend in oncology.[20–22] It was shown that near-infrared spectroscopy[23] can be employed as a noninvasive or minimally invasive diagnostics of cancer by analyzing differences of endogenous chromophores (oxygenated and deoxygenated hemoglobin, water, etc.) between normal and cancer tissues.[24] Since cancer tissues differ from normal tissues in composition, spectral information unique to each chromophore may provide a fingerprint of the disease. Hence, other benefits of spectral measurements of the prostate

*Address all correspondence to: Serge Grabtchak, E-mail: sgrabtchak@upei.ca

0091-3286/2014/$25.00

include comprehensive assessment of treatment, determination of the biomedical transparency window of the particular organ, selection of the optimal wavelength for laser treatment of benign prostatic obstruction,[25] and detection of endogenous or exogenous chromophores inside the prostate and linking them to a state of prostate health.

While the main focus of research on gold nanoparticles (NPs) for prostate cancers has been mostly on therapeutic applications,[26–28] including interstitial nanoparticle-mediated laser thermal therapy,[29,30] detection of gold nanoparticles in the prostate is a challenging and relatively unexplored topic.[29] Among the challenges are the inability to visualize and quantify the global concentration and spatial distribution of Au NPs within tumors in the prostate.[29] In addition to therapeutic applications, Au NPs can also be used for delineation of cancer regions by targeting cancer biomarkers that are overexpressed in the gland [prostate-specific membrane antigen (PSMA), for example] and then be imaged with either established clinical imaging modalities like computed tomography (CT)[31,32] or optical techniques like radiance, which is the enabling approach in the current work. In earlier work[33] we showed that optical radiance provided an improved sensitivity over CT in detection of localized inclusions of gold NPs in bulk biological tissues. While it was shown for the prostate-shaped porcine muscle phantom (mimicking the real prostate), detection of Au NPs deeply embedded in the prostate with optical radiance has never been demonstrated so far.

Radiance measures the angular distribution of photon density at the selected point in the tissue. It is interesting to note that one of the first published studies on radiance was applied to *ex vivo* human prostate.[34] However, none of the subsequent work targeted prostate applications.[35–37] Our group has introduced several novel concepts to radiance measurements, expanding capabilities of the technique and targeting prostate applications as the endpoint.[33,38–40] While these concepts have been developed and validated mostly on liquid phantoms, the utility of such combined multifunctional radiance approach for prostate applications has not been addressed until the present work.

The new method for extracting the effective attenuation coefficient and the diffusion coefficient of turbid media from relative spectrally resolved cw radiance measurements using the diffusion approximation was presented in Ref. 41. The method was validated on simulated and experimental radiance data for homogenous Intralipid-1% liquid phantom; however, it has not been applied to the prostate. Another motivation for the current work was that due to lack of published data on spectrally resolved absorption and scattering properties of canine prostate, it was not clear if one could interrogate the prostate with a low-power (<20 W) white light source at large (>1 cm) source-detector separations.

In the current work, we demonstrate the feasibility of the multifunctional radiance approach for *ex vivo* canine prostate studies advancing the approach in the following novel applications: (1) to perform minimal invasive optical interrogation of the prostate gland with a low-power white light source, (2) to provide absorption and scattering parameters of the prostate in a wide spectral range without a need for calibration, (3) to link the optical absorption coefficient to contributions of major chromophores in the prostate (oxyhemoglobin, deoxyhemoglobin, and water), and (4) to demonstrate detection capabilities of a localized optical inhomogeneity composed of Au NPs embedded in the canine prostate. We also provided a detailed analysis of information that can be obtained with and without puncturing the prostate and used for comparing similar measurements for the prostate-shaped porcine phantom.

2 Materials and Methods

2.1 *Canine Prostate Sample*

A canine prostate (Labrador retriever, intact male, 10 to 12 years, 26 kg) was harvested at the Atlantic Veterinary College, University of PEI as per Animal Control and Biosafety protocol approved by the University. The urinary bladder and proximal urethra, extending the length of the pelvic cavity and including the prostate, were removed. The ureters were transected several centimeters from the trigone, and urine was expressed from the bladder. Collection of the prostate was done ~4 h after euthanization. The largest dimension of the prostate was ~40 mm. The optical measurements began ~17 h after collection. The prostate was never frozen before or between the measurements.

2.2 *Experimental Setup*

A schematic of the experimental setup is shown in Fig. 1. The detailed description of the setup can be found in the earlier publications.[33,38,42] The prostate was held in a black plastic holder with internal diameter approximately matching the size of the prostate. To prevent the prostate from drying, distilled water was sprayed over the prostate and added to the urethra. A 20-W tungsten halogen white light source (HL-2000, Ocean Optics, Dunedin, Florida) provided tissue illumination through a fiber with a 2-mm spherical diffuser at the end. The total power output from the spherical diffuser was ~18 mW. In the absence of the well-defined rectum, the illuminating fiber was pressed against the side of the prostate with the diffuser tip positioned vertically approximately in the middle section of the prostate. Detection was performed with a custom-made 600-micron side-firing fiber (Pioneer Optics, Bloomfield, Connecticut) inserted to urethra or selected locations in the prostate and aligned vertically with the diffuser until the maximum signal was obtained. The typical insertion depth was ~17 mm. Both illuminating and detecting fibers were threaded through 15-gauge needles for mechanical stability, but only the protruding part of the detecting fiber was inserted inside the prostate to avoid self-scattering effects discussed previously.[38] The side-firing fiber was mounted on a computer-controlled rotation stage (PRM1Z8, Thorlabs, Newton, New Jersey). Radiance data were acquired by rotating the side-firing fiber over a 360-deg range with a 2-deg step. The side-firing fiber was connected to a computer-controlled spectrometer (USB 4000, Ocean Optics) that collected spectra at every angular step. It took ~4 min to acquire a complete single angular profile containing 180 spectra.

Measurements were performed at four locations in the prostate as indicated in the inset of Fig. 1. The inset shows the top view of the prostate with the position of the illuminating fiber and multiple locations of the detecting fiber with corresponding distances to the illumination point. The distances were measured with a ruler. Aside from transurethral measurements, all other interstitial measurements required puncturing prostate with a 17-gauge needle to produce a hole to accommodate the protruding part of the detecting fiber.

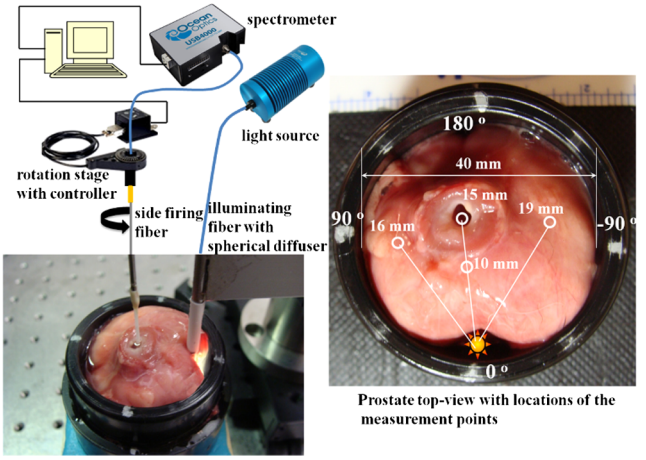

Fig. 1 The schematic of the experimental setup for radiance measurements. Inset: prostate top view with locations of the measurement points.

2.3 *Gold Nanoparticles Inclusion*

The inclusion was formed by filling a thin wall quartz capillary tube (1 mm diameter, ~30 mm height) with the colloidal solution of gold nanorods (Nanopartz) with following characteristics: plasmon resonance: 808 nm (Fig. 2); individual rod size: 10 nm (diameter) and 41 nm (length); concentration: $6.2 \cdot 10^{11}$ NPs/mL or 0.035 mg Au/mL. Molar absorption and scattering at 808 nm were $9.19 \cdot 10^8$ and $1.02 \cdot 10^8$ M^{-1} cm^{-1}, respectively, making the nanorods dominant absorbers. The inclusion contained $\sim 1.5 \cdot 10^{10}$ NPs or 0.8 μg Au in 0.024 mL volume. The inclusion was inserted in the prostate at a 10-mm distance from the urethra at a 90-deg angle with respect to the light source.

2.4 *Porcine Phantom Geometry*

On a single occasion, we performed radiance measurements in the prostate-shaped porcine muscle phantom as in Ref. 33. The prostate size piece (~4 cm diameter, ~3 cm height) was cut from the boneless pork loin and placed in the same plastic holder that accommodated the prostate (Fig. 1). Pork loin demonstrated a strong degree of heterogeneity manifested as a network of fatty inclusions between muscle fibers (see images in Ref. 33). Both detecting and illuminating fibers were inserted interstitially to the phantom with 15-mm separation keeping it in line with similar (transurethral) measurements in the prostate (position "15 mm" in the inset of Fig. 1).

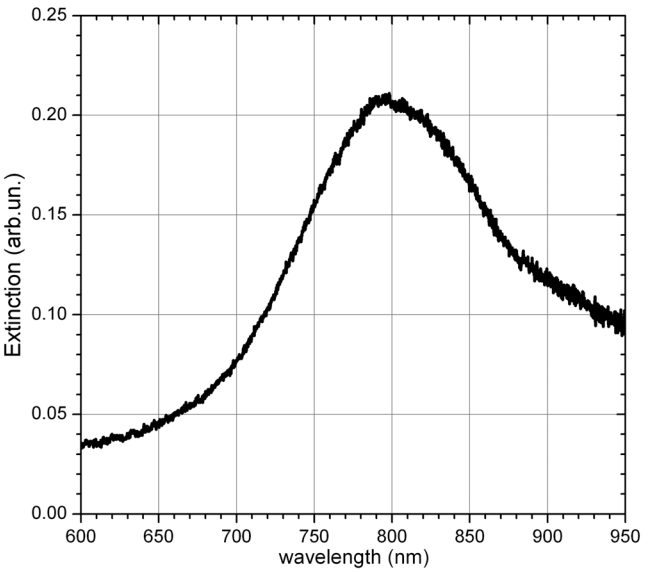

Fig. 2 The extinction spectrum of gold nanorods used in the current work.

2.5 *Data Analysis and Optical Parameters Extraction*

Optical radiance (I) is a function of the source-detector separation (r), the angle between the directions of light propagation and scattering (θ), and the wavelength of light (λ). Individual spectral profiles of radiance measured every 2 deg over 360 deg in the prostate were combined into the prostate spectro-angular matrix, $I_{\text{prostate}}(r, \theta, \lambda)$, with columns as wavelengths from 600 to 950 nm and rows as angles from −178 to 178 deg. In a similar way, the water matrix, $I_{\text{water0}}(r, \theta, \lambda)$, was assembled in which the same spectrum of radiance measured at 0 deg in water was replicated for all rows (angles) with the subscript 0 emphasizing it. Constructing a ratio of these two matrices eliminated spectral responses from the white light source, illuminating and detecting fibers in addition to referencing prostate measurements to those in water. The ratio $I_{\text{prostate}}(r, \theta, \lambda)/I_{\text{water0}}(r, \theta, \lambda)$ focuses on optical properties of the prostate, has a clear physical definition, and corresponds to relative radiance that can be, in principle, converted to the absolute value with proper normalization as was shown previously.[38] This ratio is presented via surface or contour plots demonstrating intensity and spectral variations versus angle. Such plots map the photon distribution in the angular domain and are defined as spectro-angular maps.

For detecting the presence of the localized optical inhomogeneity (inclusion) in the prostate, another ratio was constructed. As was shown earlier,[33,43] constructing the radiance extinction ratio (RER) from two radiance data sets (one for the phantom or organ with the localized inclusion and the other for the phantom or organ without the inclusion) allows isolating signatures of the inclusion from the dominant background (the prostate, in the current work) contribution, identifying it spectroscopically and locating it in the angular domain. For the inclusion of Au NPs in the prostate, the RER was defined as $\text{RER} = I_{\text{prostate}}(r, \theta, \lambda)/I_{\text{prostate+Au}}(r, \theta, \lambda)$. Hence, RER focuses on optical extinction properties of the inclusion and is presented as the contour spectro-angular plot.

Complete details of the approach for extracting optical properties can be found in Ref. 41. Only final formulas are presented here. The effective attenuation coefficient $\mu_{\text{eff}}(\lambda)$ is determined from a simple algebraic expression constructed from a ratio of two radiance measurements at two different source-detector separations (r_0 and r) and the same 90-deg angle.

$$\mu_{\text{eff}}(\lambda) = \ln[I(r, 90 \text{ deg}, \lambda) \cdot r/I(r_0, 90 \text{ deg}, \lambda) \cdot r_0]/(r_0 - r). \quad (1)$$

Then, with the knowledge of $\mu_{\text{eff}}(\lambda)$, the diffusion coefficient $D(\lambda)$ is determined from another ratio constructed from two radiance measurements at two angles (0 and 180 deg) and the same source-detector separation.

$$D(\lambda)=[1-I(r,180\,\mathrm{deg},\lambda)/I(r,0\,\mathrm{deg},\lambda)]/\{3[\mu_{\mathrm{eff}}(\lambda)+1/r][1+I(r,180\,\mathrm{deg},\lambda)/I(r,0\,\mathrm{deg},\lambda)]\}. \quad (2)$$

Once $\mu_{\mathrm{eff}}(\lambda)$ and $D(\lambda)$ are obtained, the absorption coefficient $\mu_a(\lambda)$ and the reduced scattering coefficient $\mu_s'(\lambda)$ can be determined from them as follows:

$$\mu_a(\lambda) = \mu_{\mathrm{eff}}^2(\lambda) \cdot D(\lambda), \quad (3)$$

$$\mu_s'(\lambda) = [1 - 3 \cdot \mu_{\mathrm{eff}}^2(\lambda) \cdot D^2(\lambda)]/3 \cdot D(\lambda). \quad (4)$$

The accuracy of the method depends on the accuracy of the source-detector separation measurements, which appears in the difference between two different source-detector separations (r_0 and r). For distance measurements with a ruler, the typical accuracy is ± 0.5 mm. In the worst case scenario of systematic errors, if two errors add up resulting either in the increased (± 1 mm offset) or decreased (-1 mm offset) difference, the uncertainties would be $\sim 18\%$ for $\mu_{\mathrm{eff}}(\lambda)$ and $\mu_a(\lambda)$ and $\sim 10\%$ for $D(\lambda)$ and $\mu_s'(\lambda)$. However, in practice, it is possible to keep the error for $\mu_{\mathrm{eff}}(\lambda)$ and $\mu_a(\lambda)$ <10%.

3 Results

Placing the detecting fiber in the urethra and illuminating through the rectal wall corresponds to probing the prostate in a minimally invasive way. In our experiments, such geometry was achieved by positioning the illuminating fiber at the location marked with "the sun" symbol and the detecting fiber in urethra marked with the circle labeled "15 mm" as seen in the inset of Fig. 1.

Performing a 360-deg scan in this geometry and normalizing it by the scan in water produced the spectro-angular map of relative radiance shown in Figs. 3(a) and 3(b) as contour and surface plots, respectively. Figure 3(b) accentuates the spectroscopic content. To indicate the ability of the technique to distinguish between different biological tissues, Figs. 3(c) and 3(d) present similar plots obtained at the same illumination geometry for the prostate-shaped porcine phantom.[33] Red color in all plots in Fig. 3 corresponds to the highest transmitted signal both in the spectral and angular domains.

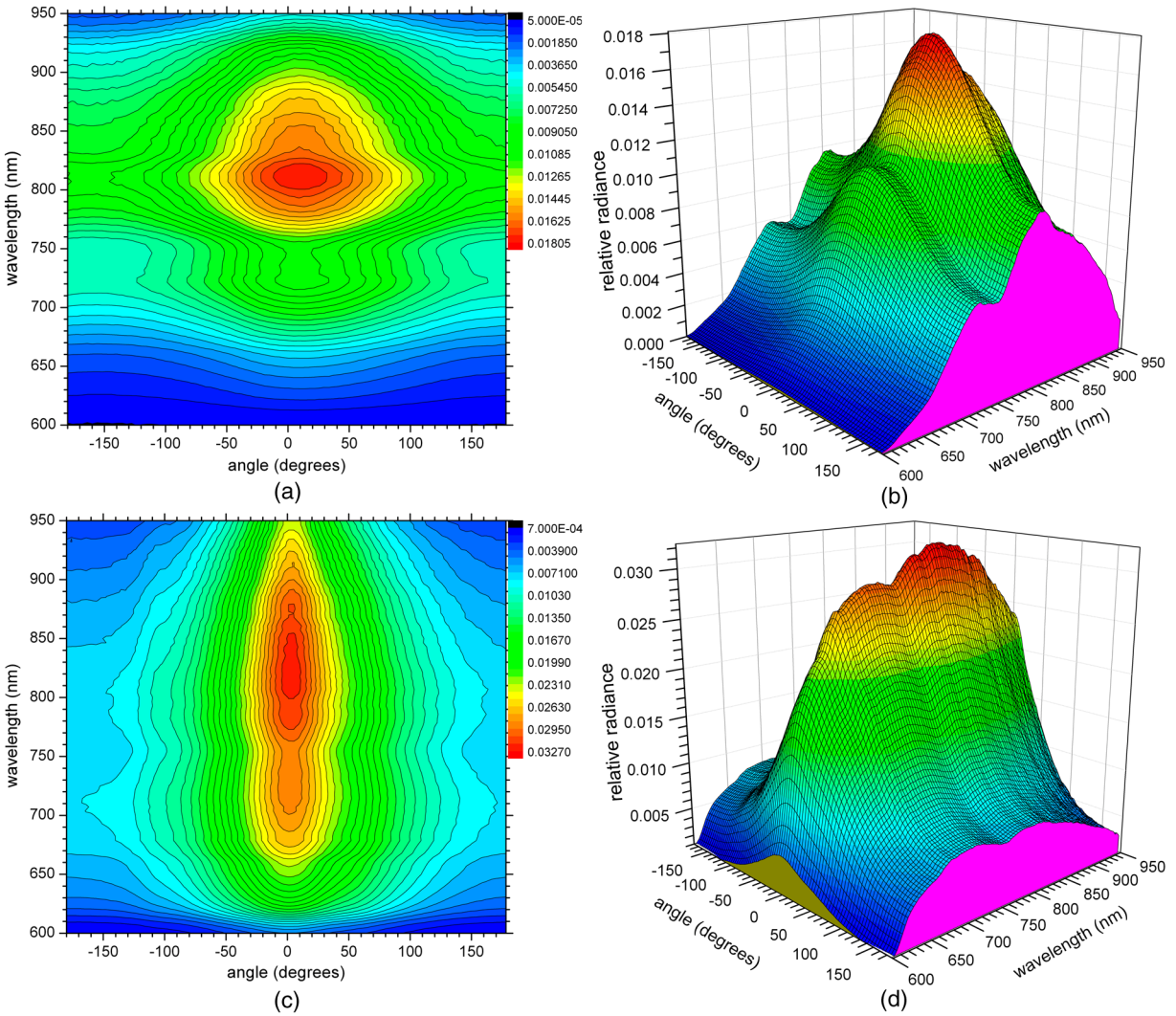

Fig. 3 Spectro-angular maps of relative radiance for canine prostate presented as contour (a) and surface (b) plots. Spectro-angular maps of relative radiance for prostate-shaped porcine phantom: (c) contour and (d) surface plots.

Two relative radiance measurements at two different source-detector separations are sufficient to extract absorption and scattering properties of the turbid medium. Three different pairs of detecting fiber positions were used for these purposes: (15 and 10 mm), (16 and 10 mm), and (19 and 10 mm) (as in the inset of Fig. 1). In the first pair, one measurement was performed via the urethra (15-mm position) and the other somewhere in the bulk prostate (10-mm position) via a needle insertion. We selected more than one probing location in different segments of the prostate (16 and 19 mm, inset of Fig. 1) to check the effect of possible heterogeneity of the sample on the measured optical properties. To restrict the influence of the urethra to a single pair (15 and 10 mm), two other pairs did not include the urethra spot but the common measurement point (10 mm) and the point in the left (16 mm) or right lobe (19 mm) of the prostate. The results of extraction of $\mu_{\text{eff}}(\lambda)$, $D(\lambda)$, $\mu_a(\lambda)$, and $\mu_s'(\lambda)$ using these pairs are presented in Figs. 4(a) to 4(d). The pair-to-pair variation of optical properties was found to be $\leq$30% for $\mu_{\text{eff}}(\lambda)$, $\leq$10% for $D(\lambda)$, $\leq$30% for $\mu_a(\lambda)$, and $\leq$10% for $\mu_s'(\lambda)$. (The experimental uncertainty for these parameters is $\leq$5% for homogenous phantoms).

Figure 5 shows the averaged experimental $\mu_a(\lambda)$ for the canine prostate across three detecting pairs. The best fit ($R^2 = 0.92$) synthetic absorption spectrum consists of 9.0($\pm$2) μM HbO_2, 29.6($\pm$0.5) μM Hb, and 0.47($\pm$0.07) fractional volume of H_2O. It corresponds to 23% oxygen saturation. The composite absorption spectrum consisting of a linear combination of multiple chromophores was constructed according to guidelines from Ref. 9. The plot also shows the individual spectra of HbO_2, Hb, and H_2O composing the final spectrum. Tabulated molar extinction coefficient for hemoglobin in water was taken from Ref. 44. The absorption coefficient of water was taken from Ref. 45. The nonlinear least-square fitting algorithm was implemented in OriginPro 8.1 (OriginLab Corp., Northampton, Massachusetts).

Figure 6 shows data on the detection of the localized inclusion made from Au NPs ($\sim 1.5 \cdot 10^{10}$ NPs or 0.8 μg Au) in the prostate positioned at a 10-mm distance from the urethra at 90-deg angle with respect to the light source position. Figure 6(a) shows RER as the contour plot. Note that red color corresponds to the region of high attenuation (extinction) of light. One can see that the area of highest extinction is located in the vicinity of

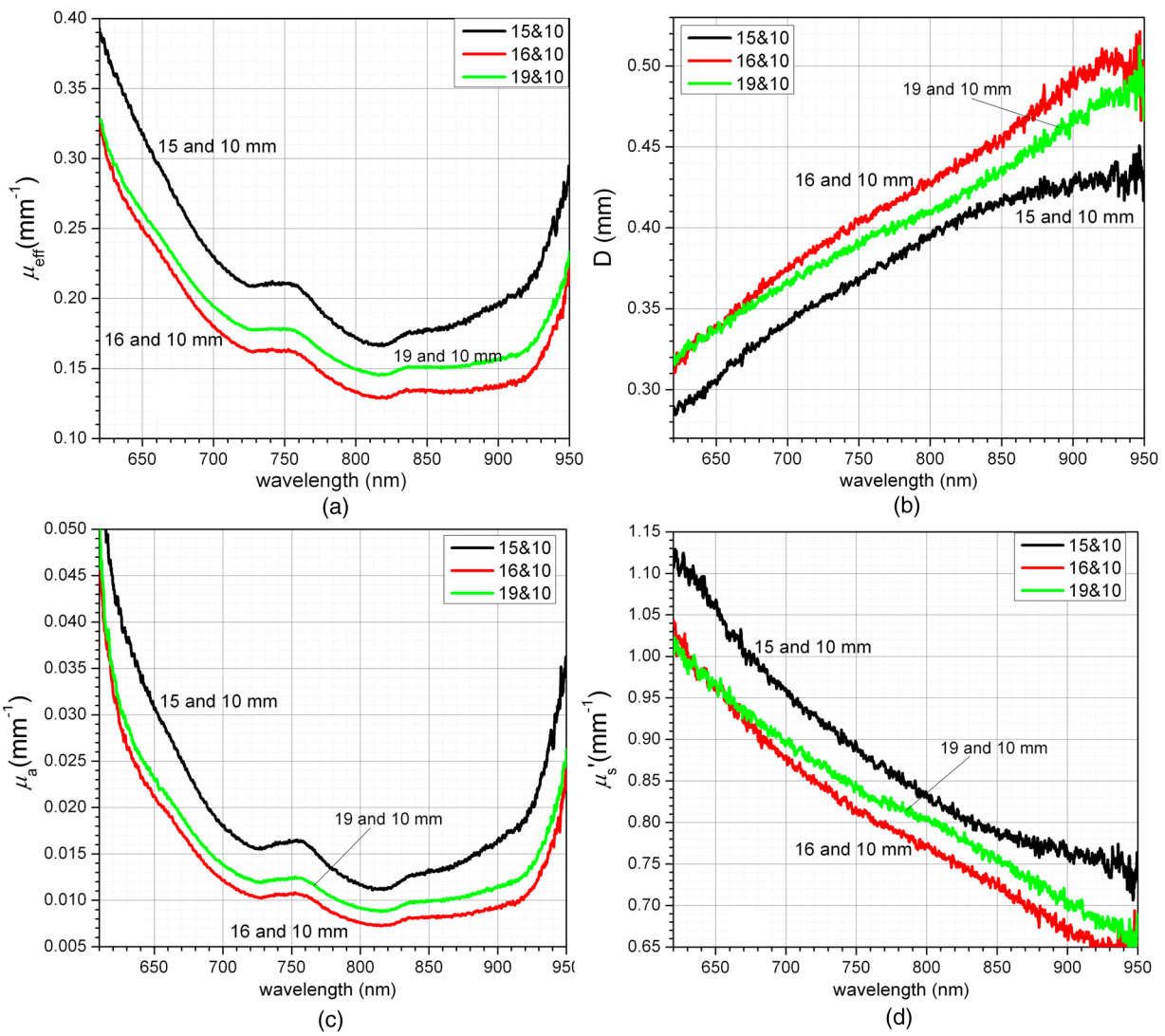

Fig. 4 Extracted optical properties of the canine prostate: (a) $\mu_{\text{eff}}(\lambda)$, (b) $D(\lambda)$, (c) $\mu_a(\lambda)$, and (d) $\mu_s'(\lambda)$.

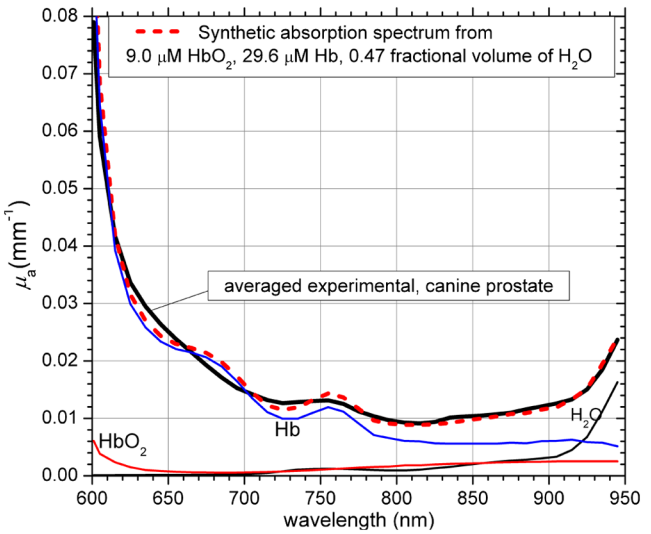

Fig. 5 Averaged ($n = 3$) extracted absorption coefficient of the canine prostate, $\mu_a(\lambda)$ matched with the synthetic absorption spectrum constructed from HbO_2, Hb, and H_2O.

90 deg in the angular domain (dotted line indicates the expected location of the target) and around 800 nm in the spectral domain. It corresponds to removal of photons approaching the detector from the direction of the inclusion. For a homogenous phantom, this would be the single feature seen in the spectro-angular map. However, the secondary area of lower intensity is also seen around −130 deg. This is an indication of phantom's heterogeneity when anisotropic scattering by local heterogeneities occurs at some preferential angles and appear as satellite (or ghost) signatures in spectro-angular maps (similar signatures were reported in Ref. 33). Figure 6(b) shows the spectrum taken along the dotted line demonstrating the characteristic absorption of gold nanorods with the plasmon resonance near 800 nm. It is close to the extinction spectrum of Au NPs obtained from standard spectroscopic measurements (Fig. 2). Thus, the spectroscopic contribution from the prostate tissue has been effectively eliminated, and the signal comes from the localized inclusion composed of Au NPs.

4 Discussion

4.1 *Analysis of Results*

Because of a large source-detector separation used in the work, photons sample a substantial portion of the prostate on a way to the detector such that their absorption and scattering are affected by interactions with the tissue in distant regions. Hence, the spectro-angular map as in Fig. 3 represents a characteristic snap-shot of bulk optical propagation in prostate tissue encoded in spectral and angular domains. Such spectro-angular mapping is obtained in a desirable minimally invasive way with the detector in the urethra and illumination near a position of the rectum. It is important to understand what information can be obtained from such measurements because this approach to canine prostate has yet to be reported.

In Fig. 3, the signal measured at 0 deg (the detector facing the light source) is composed of forward-scattered photons and can be considered as the transmission of the medium. When the detector is facing opposite to the light source (180 deg), the measured signal is composed of backscattered photons in the back-reflection geometry, while all intermediate angles provide information about other angular-sensitive pathways of photon propagation in the prostate. The maximum signal is marked with red and occurs in the forward-scattering direction (along 0 deg), which is typical for most biological tissues. The highest transmission is observed for wavelengths around 810 nm with the secondary peak of lower intensity at ~730 nm. Such shape is usually caused by overlapping transmission spectra of oxygenated and deoxygenated hemoglobin that are present in biological tissues.[33] Plots from Fig. 3 identify the spectral range of ~790 to 850 nm as the biomedical transparency window where light propagates longest distances in the excised prostate. While the concept of a generic biomedical transparency window in biological tissues is well known, possible differences in chromophore concentrations due to both morphological diversity and

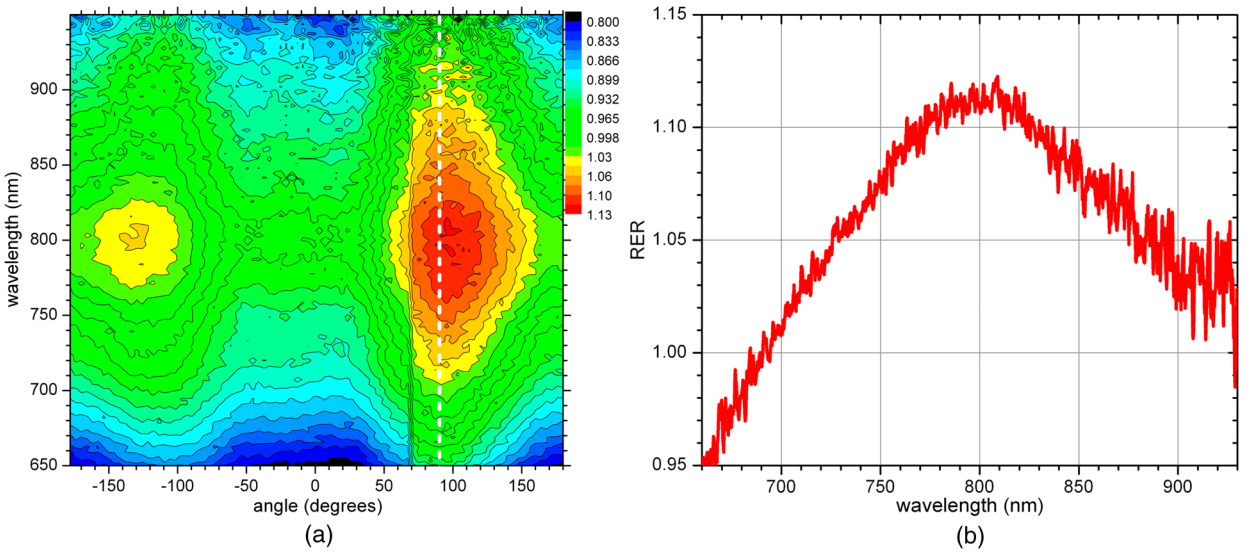

Fig. 6 Detected signatures of Au NP inclusion (composed of $1.5 \cdot 10^{10}$ Au nanorods or 0.8 μg of Au) located at 10-mm distance from urethra at 90-deg angle: (a) radiance extinction ratio (RER) as the contour plot and (b) spectrum measured along the dotted line corresponding to inclusion's direction.

Table 1 Optical properties of canine prostate from literature data.

Wavelength (nm)	$\mu_{\text{eff}}(\text{mm}^{-1})$	$\mu_s'(\text{mm}^{-1})$	$\mu_a(\text{mm}^{-1})$	Reference
630	0.5 ± 0.1	2.6 ± 2.1	0.04 ± 0.02	10 (*in vivo*)
	0.48 ± 0.09	2.6 ± 0.8	0.03 ± 0.007	(*ex vivo*)
630	0.47 ± 0.05			14 (*in vivo*)
633		2.25 ± 0.05	0.072 ± 0.007	11 (*in vitro*)
660	0.18 ± 0.04	0.92 ± 0.65	0.003 ± 0.0021	13 (capsule) (*in vivo*)
	0.206 ± 0.035	3.2 ± 2.7	0.0014 ± 0.0013	(urethra)
665	(0.011–0.273) ± 0.05			12 and 15 (*in vivo*)

pathology (as applied to prostate) would require confirming it for each sample to avoid false assignments.

A degree of ellipticity of contour lines in the horizontal direction from contour plots serves as an indicator of angular light confinement, which is broadened by multiple scattering. More elongated contour lines (consistent with higher optical scattering) also tend to bring higher values to the signal measured in the backscattered direction (at 180 deg). A simple estimation from data in Fig. 3 indicates that relative radiance in the backscattered direction drops down to ~50% of the value measured along 0 deg for the most transmitted wavelength in the canine prostate. This is slightly below the ~80% that was measured in Intralipid-1% under similar conditions.[38] It indicates qualitatively that light scattering in canine prostate is relatively strong and only marginally smaller than that in Intralipid-1%. On the other hand, multiple scattering spreads photons over the larger volume, which should facilitate detectability of localized inhomogeneities in distant regions of the sample, as was the case for detecting Au NP inclusions in Intralipid.[39]

Spatial distribution of light inside turbid media is a wavelength-dependent quantity based on absorption and scattering of individual chromophores. Even though the major chromophores in most biological tissues are the same, i.e., oxygenated (HbO_2) and deoxygenated (Hb) hemoglobin, water, lipids, etc., their concentrations differ from tissue to tissue making their combined effect on optical properties very unique for the particular tissue. To demonstrate it, Figs. 3(c) and 3(d) present the spectro-angular map in the contour and surface formats obtained for the prostate-shaped porcine muscle phantom under identical illumination/detection conditions. Other than the larger signal's intensity, the shape of the pattern is distinctly different. As expected, the maximum of intensity is detected along 0 deg. Two peaks at ~810 and ~730 nm that are well defined for the prostate have broadened, indicating a different composition of the porcine phantom. The contour lines are elongated strongly in the vertical direction with the signal measured at 180 deg down to ~30% of the signal measured along 0-deg angle. Altogether, it indicates that porcine muscle tissues exhibit less scattering than the canine prostate and light is (relatively) better confined in them. With this knowledge, we expect that localized inclusions of Au NPs in the canine prostate can be detected at larger distances (from the detector in urethra) than those reported for the porcine phantom.[33]

4.2 *Implications of the Work in Light of Other Studies*

The effect of prostate heterogeneity on optical properties manifested in up to 70% spot-to-spot variation was reported in a number of publications.[12,13] It is interesting to note that in our experiments the set involving transurethral measurements produced the highest absorption and scattering coefficients. While it may indicate different optical properties of tissues composing the urethra, more systematic measurements on a large set of samples are required to provide conclusive results. It should be noted that this radiance method does not require absolute measurements, detector calibration, or a fitting procedure for parameter extractions,[46,47] which have certain advantages.

Optical properties of the canine prostate have been the topic of a number of publications[10–19] with average values and standard deviations summarized in Table 1.

In contrast to the present study, available literature data combine *in vitro*, *ex vivo*, and *in vivo* results and refer to different but fixed wavelengths used for monitoring PDT. It is understood that these data are dependent on the sample preparation technique, prostate storage, the measurement method, and optical properties extraction algorithms in addition to instrumental errors and noise. Another important factor is prostate heterogeneity reflected in intrasample and intersample variations that can easily outweigh all other factors. A difference between *in vivo* and *ex vivo* measurements is also expected. It was suggested that postmortem tissue storage produces a decrease in $\mu_a(\lambda)$ and an increase in $\mu_s'(\lambda)$ accompanied by losses in hemoglobin.[48] Since all experimental methods have their merits, existing data cannot be ignored. With all the factors in mind, the agreement between our *ex vivo* data from the single prostate and reported discrete average values of $\mu_{\text{eff}}(\lambda)$ appears to be quite good [Fig. 7(a)]. Literature values of $\mu_a(\lambda)$ [Fig. 7(b)] and, to a greater extent, $\mu_s'(\lambda)$ [Fig. 7(c)] show a larger spread. A possible explanation is that in fluence measurements, $\mu_{\text{eff}}(\lambda)$ is determined from the slope, and thus, the values can be quite accurate. Then, since both $\mu_a(\lambda)$ and $\mu_s'(\lambda)$ contribute to $\mu_{\text{eff}}(\lambda)$, various fitting routines are used to separate them, bringing more uncertainties at this stage. In general, when comparing a discrete measurement with a continuous waveform, it might be difficult to state whether the entire curve shifted or the discrepancy occurred only at a particular wavelength.

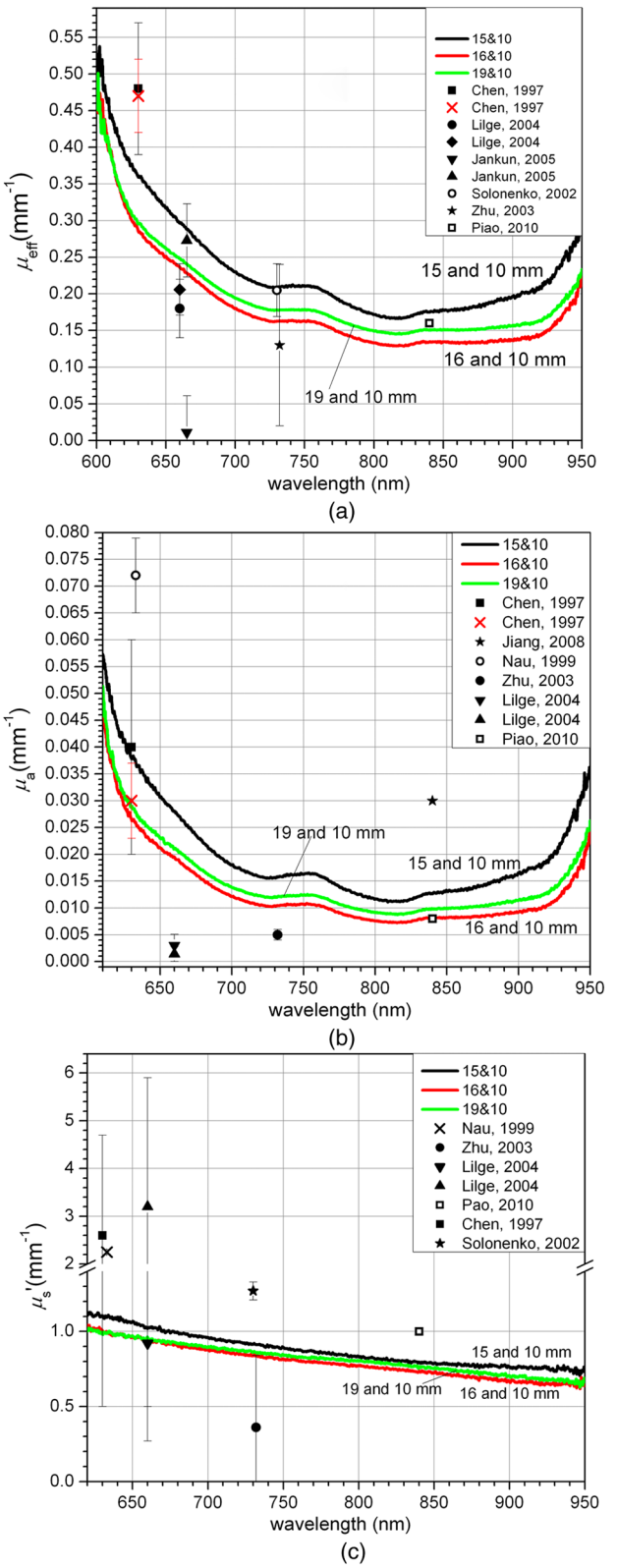

Fig. 7 Comparison of our experimental data with published values for (a) the effective attenuation coefficient, (b) absorption coefficient, and (c) reduced scattering coefficient for canine prostate.

Spectroscopic measurements provide indispensible tools for tissue characterization and diagnostics. The absorption spectrum can be linked to contributions of individual chromophores quantifying their presence in the tissue. Figure 5 shows that the spectrum of the averaged absorption coefficient of canine prostate can be matched well by the synthetic absorption spectrum composed of 9.0($\pm$2) μM of HbO_2, 29.6($\pm$0.5) μM of Hb, and 0.47($\pm$0.07) fractional volume of H_2O, which produces 38.6 μM for the total hemoglobin concentration (THC) and 23% tissue oxygen saturation (StO_2). Contributions from Hb and H_2O are associated with very distinct spectral features, while the one from HbO_2 is the lowest and provides almost constant values in the entire spectral range. Thus, the concentration of HbO_2 has the largest uncertainty (~22%). Unfortunately, such data do not exist for *ex vivo* canine prostate and are very scarce for *in vivo* canine prostate. Solonenko et al.[16] obtained 51 $\pm$ 11 μM and 50 $\pm$ 16% for THC and StO_2 correspondingly for canine prostate *in vivo*, while Jiang et al.[49] reported a wider range for THC of 110 to 150 μM also *in vivo*. While our value for THC is close to the lower end of the range reported by Solonenko et al.,[16] it is expected that *ex vivo* canine prostate would exhibit lower THC and oxygenation values as do most postmortem tissues.[48] Unfortunately, there are no studies on variation of THC and oxygenation values with time after excision for canine or human prostates. We could not find any published data on the water content in the canine prostate. However, for the human prostate, the fractional volume of water was reported to be 0.7 from *in vivo* measurements.[50–52] Water content in excised organs will depend on a number of factors, including time elapsed after extraction and organ handling, but overall, it is expected to be lower than the one obtained from *in vivo* measurements.

There are a limited number of spectroscopic studies on the water content in normal and neoplastic tissues in the prostate. This is unfortunate because this interesting chromophore may bring some promising developments in prostate cancer diagnostics. It appears from *in vitro* measurements that prostate with cancer may have lower water content than a normal prostate.[53] However, a number of *ex vivo* and *in vivo* measurements on breast[54–57] and lung[58] tumors demonstrated an increase in water content in neoplastic tissues. Thus, monitoring spectrally resolved optical properties, concentrations of major chromophores, StO_2 and water content, could offer a comprehensive approach to a systematic study of the canine prostate *ex vivo* and potentially *in vivo*. As compared with discrete wavelength measurements, the use of full spectroscopy data collection improves the accuracy of calculated values.[16,59] While THC depends on total absorption, determination of StO_2 requires detecting more subtle spectroscopic changes than are possible to derive reliably at few wavelengths.[60]

Being able to detect Au NPs in the prostate is important for their diagnostic and therapeutic applications. To the best of the authors' knowledge, detection of Au NPs in the prostate has not been reported. Figure 6 shows our data on detection of the localized inclusion made from Au NPs ($1.5 \cdot 10^{10}$ NPs or 0.8 μg of Au) in the canine prostate. Au NPs with the plasmon resonance at 808 nm were selected to fit the biomedical transparency window of the prostate (~790 to 850 nm). The position of the inclusion was chosen to match the most distant location of the inclusion that could be detected under similar conditions in the prostate-shaped porcine muscle phantom.[33] However, the diameter of the capillary was reduced from 2 to 1 mm to detect a smaller number of Au NPs, i.e., $1.5 \cdot 10^{10}$ versus $4 \cdot 10^{10}$. Detecting ~10^{10} Au NPs or ~0.8 μg of Au in 10 to 15 g prostate with a clinical CT can be quite challenging.[33] However, this number of Au NPs is very important for early detection of

cancer in the prostate when targeting PSMA receptors with Au NPs.

Receptors of PSMA are expressed in primary and metastatic prostate cancer tumors (but not in healthy vasculature)[61] at $\sim 10^6$ sites per cell.[62] Since most receptors are expressed at levels of only 10^3 to 10^4 copies per cell, it makes PSMA an attractive biomarker of prostate cancer that can be used for diagnostic and therapeutic applications. A targeted (via PSMA) delivery of gold NPs to prostate cancer cells was explored using various targeting agents: antibodies, aptamers, and small molecules.[63–66] Binding Au NPs to 1 to 10% of total PSMA receptor sites would produce $\sim 10^4$ to 10^5 Au NPs per cell. Early cancer detection requires detecting $\leq 10^5$ malignant cells (in the background of 10 to 15 g prostate), which corresponds to a transition from diffusion limited nutrition to neovascularization (labeled as angiogenic switch).[67] Hence, detecting 10^5 malignant cells with Au NPs attached to 1 to 10% of receptor sites is equivalent to detecting 10^9 to 10^{10} Au NPs in the prostate.

The reported value of detected Au NPs, $1.5 \cdot 10^{10}$, is approaching the targeted range of 10^9 to 10^{10}. It should be stressed that these numbers refer to gold nanorods used in the current work. Optical detection of Au NPs is based on the ability of NPs to absorb light that is expressed via the absorption coefficient proportional to the product of the NP concentration and the individual absorption cross-section. Here a motivation for developing new types of gold NPs for diagnostic purposes becomes very specific: NPs with absorption cross-sections larger than those of Au nanorods would require fewer total numbers in targeted prostate cancer cells in order to be detected. One of the promising candidates for this role can be gold nanocages.[68] Hence, improved sensitivity offered by optical detection may stimulate further applications of theranostic Au NPs when, for example, functionalized gold NPs targeting PSMA can be detected in the prostate and then used in NP-assisted laser thermal therapy ablating cancerous tissues.

4.3 *Methodological Limitations*

For *in vivo* applications, the experimental setup described in the current work should be modified because it was originally designed for working in liquid phantoms. Radiance detector should be placed in an external housing such that no rotating parts would be in a direct contact with tissues. Illuminating fiber with a 2-cm-long cylindrical diffuser, which is a typical fiber for PDT applications, might be a better choice than the fiber currently used. Having the cylindrical diffuser would eliminate the need of vertically aligning the detecting fiber to the illuminating fiber and provide quasi-three-dimensional sectioning capabilities by incrementally translating the detecting fiber in the vertical direction. To avoid unnecessary loss of light from the diffuser to the rectum, the cylindrical diffuser can accommodate a simplistic reflector that would direct most of the light toward the prostate.

4.4 *Future Research*

As one of the directions of future work, it would be extremely interesting to perform *in vivo* systematic radiance measurements with transurethral detection and transrectal illumination on multiple human prostates and correlate spectral and angular features with a particular state of the prostate health obtained from established methods.[69,70] Transurethral measurements with a side-firing fiber should be familiar to urologists because in the existing practice of laser prostatectomy, a side-firing fiber is already used for laser energy delivery from prostatic urethra to the adenoma for vaporization.[25]

We will also explore approaches that enable the extraction of both absorption and scattering properties of the prostate from a single spectro-angular map obtained via transurethral measurements.

Our technique offers the framework for a systematic *ex vivo* study of major chromophores in the canine and, potentially, human prostate that can be used as comprehensive diagnostic markers in determining the state of the prostate health. Hence, the technique is also well suited for elaborating the effect of postmortem prostate aging on THC and water content. Developing further theoretical aspects of the approach[40] would enable researchers to extract additional information about localized inclusions, such as concentration of Au NPs and the distance to the inclusion.

5 Conclusions

We presented a feasibility study of the multifunctional radiance-based optical platform for prostate diagnostic applications on *ex vivo* canine prostate in the minimally invasive way in the wide spectral range of 650 to 900 nm. Spectro-angular maps provided a quick qualitative assessment of optical properties of bulk tissues. For quantitative characterization, relative radiance measurements in two selected points were able to generate spectrally resolved absorption and scattering parameters for the prostate, i.e., $\mu_{\text{eff}}(\lambda)$, $D(\lambda)$,$\mu_a(\lambda)$, and $\mu_s'(\lambda)$. The absorption spectrum allowed extracting concentrations of major chromophores in the prostate: $9.0(\pm 2)$ μM of HbO_2, $29.6(\pm 0.5)$ μM of Hb, and $0.47(\pm 0.07)$ fractional volume of H_2O, which produces 38.6 μM for THC and 23% StO_2. Detection of gold nanorod inclusions containing $1.5 \cdot 10^{10}$ Au NPs or 0.8 μg of Au in the prostate was demonstrated. The number approaches the target of $\sim 10^{10}$ Au NPs that may favor early cancer detection in the prostate. The technique offers the framework for *ex vivo* systematic study of major chromophores in the canine and, potentially, human prostate that can be used as comprehensive diagnostic markers in determining the state of the prostate health. The potentials of applying the technique for *in vivo* applications were also discussed.

Acknowledgments

The authors acknowledge Dr. David R. Busch (The Children's Hospital of Philadelphia), Dr. Kai Novak (University of Heidelberg), and Dr. Jonathan Coulter (Queen's University Belfast) for useful discussions. The authors acknowledge financial support from Natural Sciences and Engineering Research Council, the Canadian Institutes of Health Research, Atlantic Canada Opportunity Agency, and Undergraduate Student Research Award from Natural Sciences and Engineering Research Council (to L.G.M). The work was also partially funded by the Canadian Research Chair Program to W.M.W.

References

1. C. L. Lai et al., "Comparative characterization of the canine normal prostate in intact and castrated animals," *Prostate* **68**(5), 498–507 (2008).
2. B. E. LeRoy and N. Northrup, "Prostate cancer in dogs: comparative and clinical aspects," *Vet. J.* **180**(2), 149–162 (2009).
3. S. L. Chowning et al., "A preliminary analysis and model of prostate injection distributions," *Prostate* **66**(4), 344–357 (2006).

4. S. Aggarwal et al., "Comparative study of PSMA expression in the prostate of mouse, dog, monkey, and human," *Prostate* **66**(9), 903–910 (2006).
5. J. M. Keller et al., "A novel canine model for prostate cancer," *Prostate* **73**(9), 952–959 (2013).
6. C. M. Moore, D. Pendse, and M. Emberton, "Photodynamic therapy for prostate cancer—a review of current status and future promise," *Nat. Clin. Pract. Urol.* **6**(1), 18–30 (2009).
7. G. Bozzini et al., "Photodynamic therapy in urology: What can we do now and where are we heading?," *Photodiagnosis Photodyn. Ther.* **9**(3), 261–273 (2012).
8. A. Gelet et al., "Transrectal high-intensity focused ultrasound: minimally invasive therapy of localized prostate cancer," *J. Endourol.* **14**(6), 519–528 (2000).
9. S. L. Jacques, "Optical properties of biological tissues: a review," *Phys. Med. Biol.* **58**(11), R37–R61 (2013).
10. Q. Chen et al., "Changes in in vivo optical properties and light distributions in normal canine prostate during photodynamic therapy," *Radiat. Res.* **147**(1), 86–91 (1997).
11. W. H. Nau, R. J. Roselli, and D. F. Milam, "Measurement of thermal effects on the optical properties of prostate tissue at wavelengths of 1,064 and 633 nm," *Lasers Surg. Med.* **24**(1), 38–47 (1999).
12. J. Jankun et al., "Diverse optical characteristic of the prostate and light delivery system: implications for computer modelling of prostatic photodynamic therapy," *BJU Int.* **95**(9), 1237–1244 (2005).
13. L. Lilge et al., "Transperineal in vivo fluence-rate dosimetry in the canine prostate during SnET2-mediated PDT," *Phys. Med. Biol.* **49**(14), 3209–3225 (2004).
14. L. K. Lee et al., "Interstitial photodynamic therapy in the canine prostate," *Br. J. Urol.* **80**(6), 898–902 (1997).
15. J. Jankun et al., "Optical characteristics of the canine prostate at 665 NM sensitized with tin etiopurpurin dichloride: need for real-time monitoring of photodynamic therapy," *J. Urol.* **172**(2), 739–743 (2004).
16. M. Solonenko et al., "In vivo reflectance measurement of optical properties, blood oxygenation and motexafin lutetium uptake in canine large bowels, kidneys and prostates," *Phys. Med. Biol.* **47**(6), 857–873 (2002).
17. T. C. Zhu et al., "In vivo optical properties of normal canine prostate at 732 nm using motexafin lutetium-mediated photodynamic therapy," *Photochem. Photobiol.* **77**(1), 81–88 (2003).
18. Z. Jiang et al., "Trans-rectal ultrasound-coupled near-infrared optical tomography of the prostate Part II: Experimental demonstration," *Opt. Express* **16**(22), 17505–17520 (2008).
19. D. Q. Piao et al., "Alternative transrectal prostate imaging: a diffuse optical tomography method," *IEEE J. Sel. Top. Quantum Electron.* **16**(4), 715–729 (2010).
20. D. J. Evers et al., "Optical spectroscopy: current advances and future applications in cancer diagnostics and therapy," *Future Oncol.* **8**(3), 307–320 (2012).
21. Q. Liu, "Role of optical spectroscopy using endogenous contrasts in clinical cancer diagnosis," *World J. Clin. Oncol.* **2**(1), 50–63 (2011).
22. P. Crow et al., "Optical diagnostics in urology: current applications and future prospects," *BJU Int.* **92**(4), 400–407 (2003).
23. P. Rolfe, "In vivo near-infrared spectroscopy," *Annu. Rev. Biomed. Eng.* **2**, 715–754 (2000).
24. V. R. Kondepati, H. M. Heise, and J. Backhaus, "Recent applications of near-infrared spectroscopy in cancer diagnosis and therapy," *Anal. Bioanal. Chem.* **390**(1), 125–139 (2008).
25. T. Bach et al., "Laser treatment of benign prostatic obstruction: basics and physical differences," *Eur. Urol.* **61**(2), 317–325 (2012).
26. D. B. Chithrani et al., "Gold nanoparticles as radiation sensitizers in cancer therapy," *Radiat. Res.* **173**(6), 719–728 (2010).
27. X. J. Zhang et al., "Enhanced radiation sensitivity in prostate cancer by gold-nanoparticles," *Clin. Investig. Med.* **31**(3), E160–E167 (2008).
28. N. Chanda et al., "Radioactive gold nanoparticles in cancer therapy: therapeutic efficacy studies of GA-198AuNP nanoconstruct in prostate tumor-bearing mice," *Nanomedicine* **6**(2), 201–209 (2010).
29. S. Krishnan, P. Diagaradjane, and S. H. Cho, "Nanoparticle-mediated thermal therapy: evolving strategies for prostate cancer therapy," *Int. J. Hyperthermia* **26**(8), 775–789 (2010).
30. J. A. Schwartz et al., "Selective nanoparticle-directed ablation of the canine prostate," *Lasers Surg. Med.* **43**(3), 213–220 (2011).
31. J. F. Hainfeld et al., "Micro-CT enables microlocalisation and quantification of Her2-targeted gold nanoparticles within tumour regions," *Br. J. Radiol.* **84**(1002), 526–533 (2011).
32. T. Reuveni et al., "Targeted gold nanoparticles enable molecular CT imaging of cancer: an in vivo study," *Int. J. Nanomed.* **6**, 2859–2864 (2011).
33. S. Grabtchak, E. Tonkopi, and W. M. Whelan, "Optical detection of gold nanoparticles in a prostate-shaped porcine phantom," *J. Biomed. Opt.* **18**(7), 077005 (2013).
34. D. J. Dickey et al., "Light dosimetry using the P3 approximation," *Phys. Med. Biol.* **46**(9), 2359–2370 (2001).
35. T. Xu et al., "Theoretical and experimental study of the intensity distribution in biological tissues," *Chin. Phys.* **14**(9), 1813–1820 (2005).
36. L. C. L. Chin et al., "Determination of the optical properties of turbid media using relative interstitial radiance measurements: Monte Carlo study, experimental validation, and sensitivity analysis," *J. Biomed. Opt.* **12**(6), 064027 (2007).
37. L. C. L. Chin et al., "Interstitial point radiance spectroscopy of turbid media," *J. Appl. Phys.* **105**(10), 102025 (2009).
38. S. Grabtchak et al., "Experimental spectro-angular mapping of light distribution in Intralipid-1%," *J. Biomed. Opt.* **17**(6), 067007 (2012).
39. S. Grabtchak, T. J. Palmer, and W. Whelan, "Radiance spectroscopy tool box for characterizing Au nanoparticles in tissue mimicking phantoms as applied to prostate," *J. Cancer Sci. Ther.* **3**(Suppl. 1), 1–7 (2011).
40. S. Grabtchak, K. Callaghan, and W. M. Whelan, "Tagging photons with gold nanoparticles as localized absorbers in optical measurements in turbid media," *Biomed. Opt. Express* **4**(12), 2989–3006 (2013).
41. S. Grabtchak and W. M. Whelan, "Separation of absorption and scattering properties of turbid media using relative spectrally resolved cw radiance measurements," *Biomed. Opt. Express* **3**(10), 2371–2380 (2012).
42. S. Grabtchak, T. J. Palmer, and W. M. Whelan, "Detection of localized inclusions of gold nanoparticles in Intralipid-1% by point-radiance spectroscopy," *J. Biomed. Opt.* **16**(7), 077003 (2011).
43. S. Grabtchak et al., "Radiance detection of non-scattering inclusions in turbid media," *Biomed. Opt. Express* **3**(11), 3001–3011 (2012).
44. S. Takatani and M. D. Graham, "Theoretical analysis of diffuse reflectance from a 2-layer tissue model," *IEEE Trans. Biomed. Eng.* **BME-26** (12), 656–664 (1979).
45. D. J. Segelstein, *The Complex Refractive Index of Water*, p. 167, University of Missouri, Kansas City (1981).
46. T. C. Zhu, J. C. Finlay, and S. M. Hahn, "Determination of the distribution of light, optical properties, drug concentration, and tissue oxygenation in-vivo in human prostate during motexafin lutetium-mediated photodynamic therapy," *J. Photochem. Photobiol. B-Biol.* **79**(3), 231–241 (2005).
47. T. C. Zhu and J. C. Finlay, "Prostate PDT dosimetry," *Photodiagnosis Photodyn. Ther.* **3**(4), 234–246 (2006).
48. A. Roggan et al., "The effect of preparation technique on the optical parameters of biological tissue," *Appl. Phys. B* **69**(5–6), 445–453 (1999).
49. Z. Jiang et al., "Trans-rectal ultrasound-coupled spectral optical tomography of total hemoglobin concentration enhances assessment of the laterality and progression of a transmissible venereal tumor in canine prostate," *Urology* **77**(1), 237–242 (2011).
50. T. Svensson et al., "In vivo optical characterization of human prostate tissue using near-infrared time-resolved spectroscopy," *J. Biomed. Opt.* **12**(1), 014022 (2007).
51. T. Svensson et al., "Towards accurate in vivo spectroscopy of the human prostate," *J. Biophotonics* **1**(3), 200–203 (2008).
52. M. S. Thompson et al., "Clinical system for interstitial photodynamic therapy with combined on-line dosimetry measurements," *Appl. Opt.* **44**(19), 4023–4031 (2005).
53. J. H. Ali et al., "Near infrared spectroscopy and imaging to probe differences in water content in normal and cancer human prostate tissues," *Technol. Cancer Res. Treat.* **3**(5), 491–497 (2004).
54. L. Spinelli et al., "Bulk optical properties and tissue components in the female breast from multiwavelength time-resolved optical mammography," *J. Biomed. Opt.* **9**(6), 1137–1142 (2004).
55. B. W. Pogue et al., "Characterization of hemoglobin, water, and NIR scattering in breast tissue: analysis of intersubject variability and menstrual cycle changes," *J. Biomed. Opt.* **9**(3), 541–552 (2004).

56. D. Hsiang et al., "In vivo absorption, scattering, and physiologic properties of 58 malignant breast tumors determined by broadband diffuse optical spectroscopy," *J. Biomed. Opt.* **11**(4), 044005 (2006).
57. S. H. Chung et al., "In vivo water state measurements in breast cancer using broadband diffuse optical spectroscopy," *Phys. Med. Biol.* **53**(23), 6713–6727 (2008).
58. K. Nowak et al., "Intraoperative lung edema monitoring by microwave reflectometry," *Interact. Cardiovasc. Thorac. Surg.* **12**(4), 540–544 (2011).
59. R. M. P. Doornbos et al., "The determination of in vivo human tissue optical properties and absolute chromophore concentrations using spatially resolved steady-state diffuse reflectance spectroscopy," *Phys. Med. Biol.* **44**(4), 967–981 (1999).
60. L. C. Enfield and A. P. Gibson, "A review of mechanisms of contrast for diffuse optical imaging of cancer," *J. Near Infrared Spectrosc.* **20**(1), 185–202 (2012).
61. S. S. Chang et al., "Prostate-specific membrane antigen is produced in tumor-associated neovasculature," *Clin. Cancer Res.* **5**(10), 2674–2681 (1999).
62. P. M. Smith-Jones et al., "In vitro characterization of radiolabeled monoclonal antibodies specific for the extracellular domain of prostate-specific membrane antigen," *Cancer Res.* **60**(18), 5237–5243 (2000).
63. D. J. Javier et al., "Aptamer-targeted gold nanoparticles as molecular-specific contrast agents for reflectance imaging," *Bioconjug. Chem.* **19**(6), 1309–1312 (2008).
64. D. Kim, Y. Y. Jeong, and S. Jon, "A drug-loaded aptamer-gold nanoparticle bioconjugate for combined CT imaging and therapy of prostate cancer," *ACS Nano* **4**(7), 3689–3696 (2010).
65. B. B. Kasten et al., "Targeting prostate cancer cells with PSMA inhibitor-guided gold nanoparticles," *Bioorg. Med. Chem. Lett.* **23**(2), 565–568 (2013).
66. D. Schol et al., "Anti-PSMA antibody-coupled gold nanorods detection by optical and electron microscopies," *Micron* **50**, 68–74 (2013).
67. J. V. Frangioni, "New technologies for human cancer imaging," *J. Clin. Oncol.* **26**(24), 4012–4021 (2008).
68. J. Y. Chen et al., "Gold nanocages: engineering their structure for biomedical applications," *Adv. Mater.* **17**(18), 2255–2261 (2005).
69. S. Eggener et al., "Focal therapy for prostate cancer: possibilities and limitations," *Eur. Urol.* **58**(1), 57–64 (2010).
70. M. J. Manyak et al., "The evolution of imaging in advanced prostate cancer," *Urol. Clin. N. Am.* **33**(2), 133–146 (2006).

Biographies of the authors are not available.